Performance of almost edgeless silicon detectors in CTS and 3D-planar technologies

2013 JINST 8 P06009

(http://iopscience.iop.org/1748-0221/8/06/P06009)

PUBLISHED BY IOP PUBLISHING FOR SISSA MEDIALAB

RECEIVED: *April 9, 2013*
ACCEPTED: *May 14, 2013*
PUBLISHED: *June 14, 2013*

Performance of almost edgeless silicon detectors in CTS and 3D-planar technologies

The TOTEM collaboration

E. Alagoz,[a] G. Anelli,[a] G. Antchev,[a] V. Avati,[a] V. Bassetti,[b] V. Berardi,[c] V. Boccone,[b] M. Bozzo,[b] E. Brücken,[d] A. Buzzo,[b] M.G. Catanesi,[c,1] S. Cuneo,[b] C. Da Via,[e,2] M. Deile,[a] R. Dinapoli,[a] K. Eggert,[a] V. Eremin,[f] F. Ferro,[b] J. Hasi,[e,2] F. Haug,[a] J. Heino,[d] P. Jarron,[a] J. Kalliopuska,[d] J. Kašpar,[a,g] C. Kenney,[h] A. Kok,[e,2] V. Kundrát,[g] K. Kurvinen,[d] R. Lauhakangas,[d] E. Lippmaa,[l] M. Lokajíček,[g] T. Luntama,[d] D. Macina,[a] M. Macrí,[b] S. Minutoli,[b] L. Mirabito,[a] H. Niewiadomski,[a] E. Noschis,[a] F. Oljemark,[d] R. Orava,[d] M. Oriunno,[a] K. Österberg,[d] S. Parker,[i] A.-L. Perrot,[a] E. Radermacher,[a] E. Radicioni,[c] G. Ruggiero,[a] H. Saarikko,[d] A. Santroni,[b] G. Sette,[b] P. Siegrist,[a] J. Smotlacha,[g] W. Snoeys,[a] C. Taylor,[j] S. Watts[e,2] and J. Whitmore[k]

[a] *CERN, 1211 Genève 23, Switzerland*
[b] *INFN Sezione di Genova and Università di Genova, Via Dodecaneso 33, 16146 Genova, Italy*
[c] *INFN Sezione di Bari and Politecnico di Bari, Via Orabona 4, 70126 Bari, Italy*
[d] *Helsinki Institute of Physics and Department of Physical Sciences, University of Helsinki, P.O. Box 64, 00014 Helsinki, Finland*
[e] *Brunel University, Uxbridge, Middlesex UB8 3PH, U.K.*
[f] *Ioffe Physico-Technical Institute, Polytechnicheskaya Str. 26, 194021 St-Petersburg, Russia*

[1] Corresponding author.
[2] Now at the University of Manchester, U.K.

doi:10.1088/1748-0221/8/06/P06009

2013 JINST 8 P06009

[g]*Institute of Physics ASCR ,*
Na Slovance 1999, 182 21 Praha, Czech Republic
[h]*Molecular Biology Consortium, Stanford Nanofabrication Facility,*
Palo Alto, CA 94303, U.S.A
[i]*University of Hawaii, c/o Lawrence Berkeley Laboratory,*
Berkeley, CA 94720, U.S.A.
[j]*Department of Physics, Case Western Reserve University,*
Cleveland, OH 44106, U.S.A.
[k]*Department of Physics, Penn State University,*
University Park, PA 16802, U.S.A.
[l]*National Institute of Chemical Physics and Biophysics NICPB,*
Tallinn, Estonia

E-mail: gabriella.catanesi@cern.ch

ABSTRACT: The physics programme of the TOTEM experiment requires the detection of very forward protons scattered by only a few microradians out of the LHC beams. For this purpose, stacks of planar Silicon detectors have been mounted in moveable near-beam telescopes (Roman Pots) located along the beamline on both sides of the interaction point. In order to maximise the proton acceptance close to the beams, the dead space at the detector edge had to be minimised. During the detector prototyping phase, different sensor technologies and designs have been explored. A reduction of the dead space to less than 50 μm has been accomplished with two novel silicon detector technologies: one with the Current Terminating Structure (CTS) design and one based on the 3D edge manufacturing. This paper describes performance studies on prototypes of these detectors, carried out in 2004 in a fixed-target muon beam at CERN's SPS accelerator. In particular, the efficiency and accuracy in the vicinity of the beam-facing edges are discussed.

KEYWORDS: Particle tracking detectors (Solid-state detectors); Particle tracking detectors

2013 JINST 8 P06009

Contents

2013 JINST 8 P06009

1 Introduction

In general, planar silicon detectors have a wide (typically 1 mm) insensitive border around the active area, occupied by a sequence of guard rings that control the potential distribution between the detector's sensitive area and the die cut. Such a large insensitive near-edge area was unacceptable for the TOTEM experiment [1, 2] at the interaction point 5 of the LHC. TOTEM's primary goal, the precise measurement of the total pp cross-section, requires the measurement of elastically or diffractively produced very forward protons, scattered by merely a few microradians out of the high-intensity beams. The trajectories of these particles, determined mainly by their scattering angles and momentum losses in conjunction with the LHC lattice configuration [3], are measured by silicon detectors placed between 5 and 10 times the transverse (1-sigma) beam size from the beam centre. The influence of the near-edge insensitive volume on the proton acceptance can be quantified by the lowest detectable scattering angle, given in table 1.

The running scenarios presented in table 1 are characterised by the betatron function β^* at the interaction point, which — for a given transverse emittance — determines the beam size and hence defines the smallest tolerable Roman Pot distance to the beam centre. The width of the insensitive edge area becomes particularly crucial for the $\beta^* = 1535$ m optics, foreseen in the ultimate TOTEM

Table 1. Smallest detected scattering angle Θ_{min} in the vertical RPs installed at 220 m from IP5 in case of fully sensitive detectors ($d = 0$) and in case of standard planar silicon detectors with an insensitive near-edge zone of $d = 1$ mm width. The values are given for three typical running scenarios [2] characterised by the betatron function β^* in the vertex and by the normalised transverse emittance ε_n. In all cases, a centre-of-mass energy $\sqrt{s} = 14$ TeV and a detector distance of $10\,\sigma$ from the beam centre are assumed.

β^* [m]	ε_n [μm rad]	$10\,\sigma$ vert. beam size [mm]	Θ_{min} $d = 0$ [μrad]	Θ_{min} $d = 1$ mm [μrad]
2	3.75	3.15	173	227
90	3.75	6.25	24	27
1535	1	0.81	3.0	6.6

running scenario for the most precise total pp cross-section measurement at $\sqrt{s} = 14$ TeV. For this lattice configuration, the horizontal and vertical beam sizes at 220 m from the interaction region are only 30 μm and 81 μm, respectively. In case of a typical 1 mm-wide insensitive edge volume and a 10 beam standard deviation detector approach, the smallest detected angle is 6.6 μrad compared to 3 μrad for a 50 μm dead space, corresponding to a minimum observable four-momentum transfer $|t|_{\text{min}} = \Theta^2_{\text{min}} p^2 = 19 \times 10^{-4}\,\text{GeV}^2$ instead of $4 \times 10^{-4}\,\text{GeV}^2$.

The TOTEM collaboration has therefore investigated two novel techniques for microstrip sensors: the Current Terminating Structure (CTS) [4, 5] and the 3D-planar detector with active edges [6].

2 Edgeless silicon detectors

2.1 Current terminating structure (CTS)

The CTS [1, 2, 4, 5] and its biassing scheme are shown in figure 1. The basic idea of the CTS approach is to reduce the insensitive border below 100 μm by applying a large fraction of the detector bias across the detector chip cut through an outer current terminating ring (CTR) that collects the major part of the resulting surface-generated current I_{CTR}. A ring placed between the CTR and the strips, called clean-up ring (CR), is biased at the same potential as the CTR. The leakage current ICR collected at the CR consists mainly of a small fraction of the current generated at the cut surface due to diffusion. This structure decouples the high leakage current generated at the detector cut edge from the sensitive volume. The strips are biased by punch-through between the biasing electrode and the strips.

First samples of silicon detectors with CTS have been developed in a joint effort between the TOTEM group at CERN and Megaimpulse, a spin-off company from the Ioffe PT Institute in St. Petersburg (Russia). The 350 μm thick prototypes covering an area of $1.2 \times 1.2\,\text{mm}^2$ were successfully tested in September 2003 with a muon beam in the SPS fixed target beam line X5 at CERN [4, 5]. The detectors exhibited an insensitive margin of at most 60 μm width. Based on this experience, final-size detectors (300 μm thick, with an area of $3.5 \times 3.5\,\text{cm}^2$) were developed

2013 JINST 8 P06009

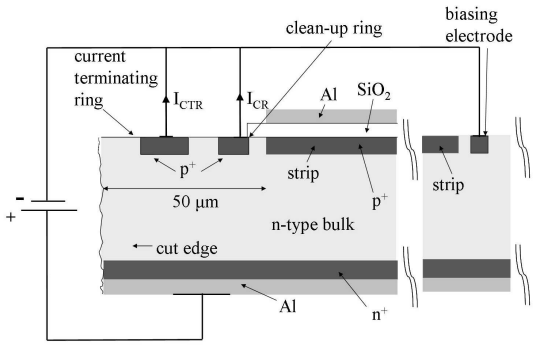

Figure 1. Cross-section and biassing scheme of a CTS-edge silicon detector with its electrodes: the biassing electrode, the current terminating ring (CTR) and the clean-up ring (CR).

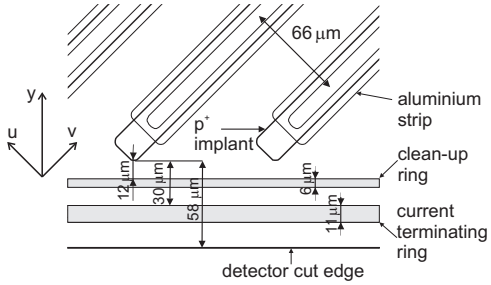

Figure 2. CTS Detector edge layout. The strips are tilted at 45° with respect to the edge.

and extensively studied in X5 [3]. In particular, the tracking capabilities and the efficiency in the near-edge area (see figure 2) were analysed in detail with a ∼100 GeV muon beam and are reported in the following sections.

2.2 3D-planar detector technology

In the 3D-planar silicon devices the central part is also, as in the case of the CTS sensors, a planar microstrip detector, while the edge is fabricated using 3D processing [7–9]. In this configuration, the free edges of the planar sensor are deep etched and n^+ dopant is diffused in. Then the sensor is removed from the wafer, again by etching, thus avoiding the typical surface defects produced by saw cuts. In this way the edges become an extension of the back-side n^+ electrode [6], as shown schematically in figure 3. The enclosing n^+ electrode — the "active edge" — completely defines the electric field distribution when a reverse bias voltage is applied. The potential difference is not applied along the cut edge from the back plane to the front plane, but across the 33 μm-wide gap between the n^+ doped active edge (5 μm thick) and the strip end. The gap between the edge electrode and the strips is passivated by phosphorus to further reduce the leakage current and to increase the breakdown voltage.

As a result of 3D edge manufacturing, the surface leakage current, usually present after a device has been saw-cut, is suppressed. Moreover, the sensor is now active up to a few microns from the edge.

2013 JINST 8 P06009

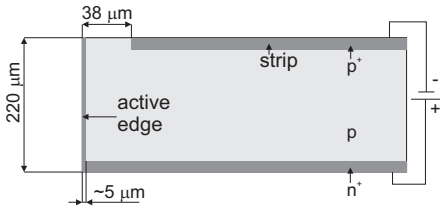

Figure 3. Sketch of a planar-3D detector as used in the beam tests discussed in this article. The edge on the left-hand side is an extension of the back-side n^+ electrode.

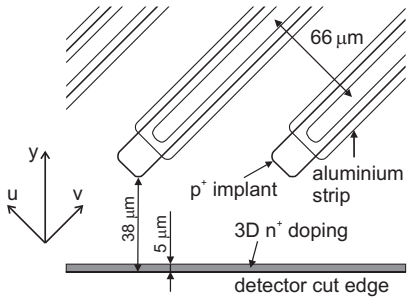

Figure 4. 3D-planar detector active edge layout. The strip direction has an angle of 45° with respect to the edge.

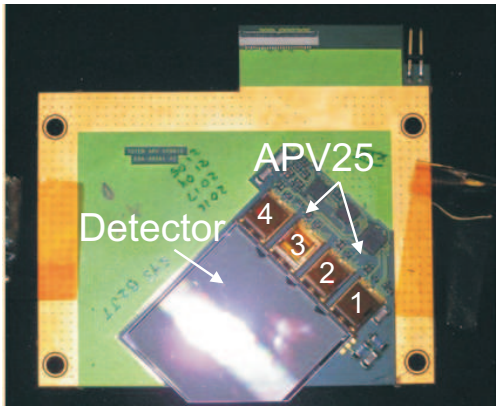

Figure 5. Picture of a hybrid board with a planar microstrip detector, $3.4 \times 3.4\,\mathrm{cm}^2$ large, mounted on it. The detector is connected electrically to four APV25 readout chips via wire bonds.

Prototypes of 3D-planar sensors ($220\,\mu$m thick, covering an area of $3.4 \times 3.4\,\mathrm{cm}^2$) were studied in the same beam tests as the CTS devices discussed in section 2.1. The layout of the near-edge region is shown in figure 4.

3 Detector test setup

The CTS and 3D-planar silicon detectors under test were sized and shaped according to the TOTEM specifications [2]. They were segmented in 512 strips of $66\,\mu$m pitch. Each detector was glued to a PCB ("hybrid board", see figure 5) and bonded to four read-out chips.

2013 JINST 8 P06009

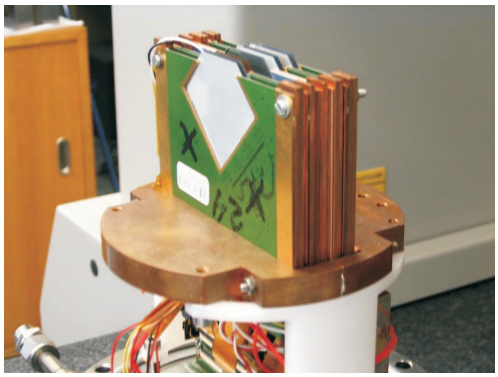

Figure 6. Package of 8 hybrids.

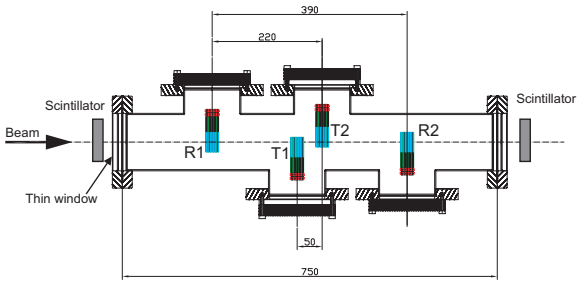

Figure 7. Arrangement of the test (T1, T2) and reference (R1, R2) packages inside a vacuum tube.

The sensors were assembled in four packages (figure 6), each consisting of four pairs of hybrids. The two hybrids of each pair were mounted back-to-back, thus having orthogonal strip directions, called *u* and *v*. The majority (24 detectors) was read out with CMS's analogue APV25 chips [12, 13], while a few were equipped with prototypes of TOTEM's own newly developed digital front-end chip VFAT [14].

The four packages formed a telescope placed inside a vacuum tube, as drawn in figure 7. Two packages acted as reference detectors to define the muon tracks while the other two packages in the centre contained the detectors to be studied. The tracking information was calculated on the basis of the strip hits acquired through the APV25 chips and the associated analogue readout electronics [15]. The CTS and 3D-planar detectors were operated at a bias voltage of 40 V and 30 V, respectively, and at a temperature of $-10\,^{\circ}$C.

4 Alignment

The positions of all the detectors had to be determined to a precision better than the detector resolution. Since the theoretical resolution $\sigma_{x,y}$ of a 66 μm pitched strip detector without charge sharing is $66\,\mu\text{m}/\sqrt{12} = 19.1\,\mu\text{m}$, the optimal achievable interpolation resolution in the centre between the reference packages was about 9 μm.

The alignment of the detectors was accomplished with metrology measurements and with a software algorithm based on reconstructed muon tracks.

2013 JINST 8 P06009

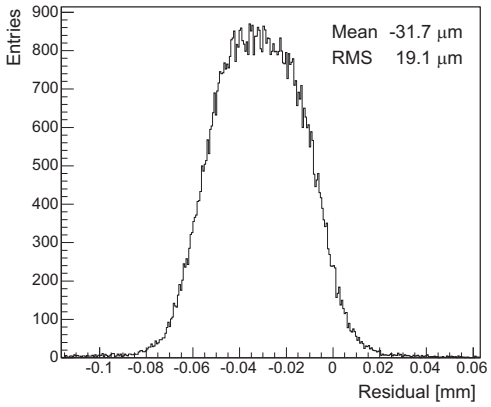

Figure 8. Track reconstruction residual distribution (impact position – track intercept with the detector) in the readout direction of CTS detector 11 if only metrology measurements are taken into account.

4.1 Metrology measurements

The metrology measurements using optical and mechanical instruments allowed for a determination of the sensor positions to an accuracy of only a few tens of microns. This is illustrated by a residual distribution of reconstructed tracks in one typical detector (figure 8). The histogram reveals a detector shift of $32\,\mu$m. The rms value of $19.1\,\mu$m — consistent with the pure one-strip resolution — indicates that the rotation misalignment is small. As expected, the observed distribution is not gaussian but a smeared box distribution.

4.2 Software alignment

The muon tracks in the SPS test beam were perpendicular to the detector planes, with a beam divergence of less than 1 mrad. Due to negligible multiple scattering of about $0.1\,\mu$rad per silicon detector, the particle trajectories are fitted with straight lines in the coordinate system of the telescope. Its x and y coordinates were defined transverse to the beam running in the positive z direction. The objective of the alignment procedure was to find the displacements $(\Delta x_i, \Delta y_i)$ and the rotations $\Delta\gamma_i$ about the z-axis of the individual sensors relative to their nominal positions and orientations. Since the detector packages were composed of pairs of hybrids with orthogonal strips, the full three-dimensional track reconstruction was possible.

The impact points used in the analysis were reconstructed on the basis of the analogue information from the APV25 chips after a signal-to-noise cut $S/N > 4$. The impact position was reconstructed with a centre-of-gravity algorithm [16] acting on clusters of adjacent strip hits weighted with their signal amplitudes. The tracks were reconstructed by minimisation of χ^2, defined as

$$\chi^2 = \vec{\varepsilon}^{\,\mathrm{T}} \mathbf{V}^{-1} \vec{\varepsilon}\,, \tag{4.1}$$

where $\mathbf{V}$ is the covariance matrix of the measurements and $\vec{\varepsilon}$ is a vector of residuals, defined as the difference between the impact position and the reconstructed track intersection with the detector plane.

In the alignment procedure only tracks traversing all the available detectors were used. The precision of the detector alignment obtained with "Grand χ^2" minimisation, i.e. fitting misalignment and track parameters simultaneously, was considerably better than the detector resolution, as

2013 JINST 8 P06009

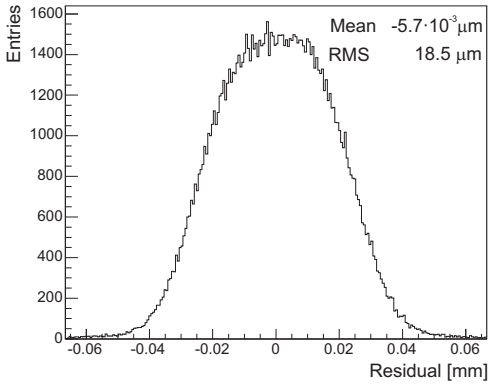

Figure 9. The residual distribution (CTS detector 11) after software alignment.

can be seen in figure 9. In contrast to figure 8, the mean value is now close to 0, which indicates that the displacements were correctly determined, allowing an optimal interpolation precision in the efficiency and resolution studies.

The *y*-position of each detector's critical edge was determined by a combination of mechanical measurements and tracking information with a precision of 7–14 μm.

5 Detector performance

Four CTS detectors (listed in table 2) and one 3D-planar detector were used for the performance tests.

All CTS devices were operated at a reverse bias of 40 V and exhibited similar behaviour. In the following sections detector 11 will be discussed in more detail, whereas summary results are presented for all the detectors.

The 3D-planar prototype detector was operated slightly under-depleted at a reverse bias voltage of 30 V. This choice was made because of a large leakage current injected by a noisy strip and possible break-down at higher bias voltages.

5.1 Signal-to-noise ratio

Figure 10 shows the signal-to-noise distribution of the CTS detector 11 without applying any reconstruction cuts. The signal peak with a most probable value of 17 is well separated from the noise pedestal, resulting in a high detector efficiency. When the same detector was operated at a higher reverse bias of 100 V, this value increased to 27. The signal-to-noise dependence upon the bias voltage is discussed in more detail in [17].

The signal-to-noise distribution of the 3D-planar detector is shown in figure 11. Due to the limited allowable bias range and the sensor thickness of only 220 μm, the most probable value of the signal-to-noise ratio was 10.5, leading to a slightly reduced efficiency for this early prototype detector.

5.2 Edge efficiency

Efficiency studies were performed by reconstructing tracks with the reference detectors and comparing their predicted impact points in the test detectors with the actual response. The track effi-

2013 JINST 8 P06009

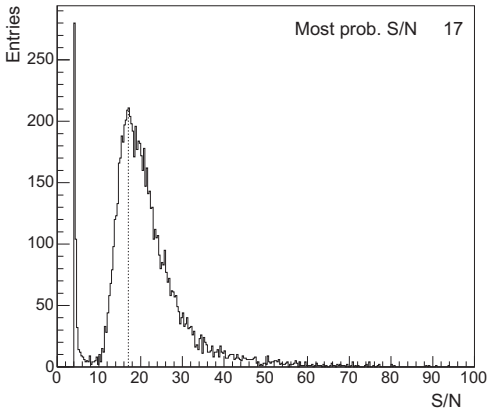

Figure 10. Signal-to-noise (S/N) distribution of the tested CTS detector 11 operated at 40 V and -10°C without any reconstruction cuts.

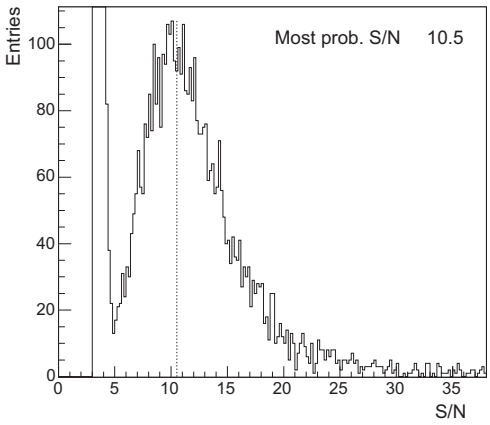

Figure 11. Signal-to-noise profile of the tested 3D-planar detector operated at 30 V without any reconstruction cuts.

ciency close to the cut edge was determined as a function of the y-coordinate that is parallel to the detector plane and perpendicular to the critical detector edge. The edge efficiency profile of the CTS detector 11 is shown in figure 12. The profile was fitted with

$$\eta(y) = \frac{\eta_0}{2}\left[1 + \mathrm{Erf}\left(\frac{y - y_0}{\sigma_y\sqrt{2}}\right)\right], \tag{5.1}$$

where Erf is the Gaussian error function, η_0 is the plateau efficiency, y_0 is the 50 % efficiency position, and σ_y represents the width of the efficiency rise interval (with a contribution from the track interpolation error). The details of the fits for all the tested CTS detectors are summarised in table 2.

The efficiency was observed to rise from 10 to 90 % of its plateau value within 34 μm on average, with an rms spread of 7 μm between the individual sensors. As described in the previous chapter, the track interpolation uncertainty is about 9 μm, which would by itself lead to a $(10-90)$% rise interval of 23 μm. Deconvolution of this smearing yields a pure efficiency rise interval of 23 μm average width. The distance between the cut edge — known with a precision between 7 and

2013 JINST 8 P06009

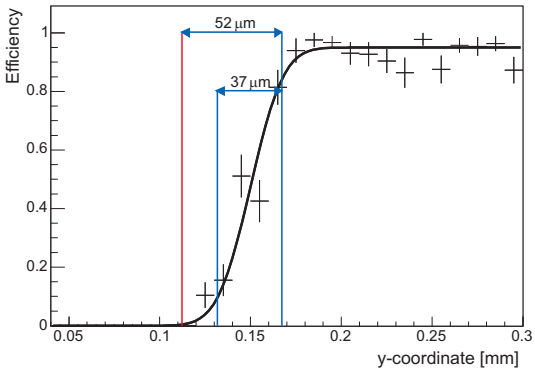

Figure 12. The efficiency profile at the special edge of the CTS detector 11. The left-most red vertical line gives the position of the wafer cut. The blue lines show the 10–90 % efficiency rise interval. The fit details are given in table 2.

Table 2. Results of the edge efficiency studies of the four tested CTS detectors. The errors in the "mean" row represent the rms spread of the four samples.

Det. id.	(10 –90) % eff. rise interval $d_{10-90\%}$ [μm]	Cut edge to 90 % eff. dist. $d_{\mathrm{cut}-90\%}$ [μm]	Efficiency plateau η_0 [%]	χ^2/ndf
7	43 ± 3	62 ± 13	96.7 ± 0.5	40 / 57
11	37 ± 3	52 ± 14	95.3 ± 0.6	57 / 61
12	27 ± 3	45 ± 14	94.1 ± 1.0	38 / 57
13	27 ± 3	45 ± 7	93.8 ± 0.8	53 / 51
mean $\pm$rms	34 ± 7	51 ± 7	95.0 ± 1.1	

14 μm — and the 90 % efficiency point was found to be on average 51 μm with a spread of 7 μm. After correction for the interpolation smearing, this distance amounts to 47 μm. The efficiency plateau for all the detectors has a level of about 95 %, where the missing 5 % were caused mainly by 4 unbonded and typically 2 noisy strips out of the 208 strips covering the critical edge.

The efficiency profile of the 3D-planar detector's active edge is shown in figure 13. The efficiency rises from 10 to 90 % within 24 μm. Given the extrapolation accuracy of 9 μm as discussed for the CTS detectors, the $(10-90)\%$ interval of the test device alone is only 7 μm wide. This steep efficiency increase is likely to start directly at the cut edge, but the metrology uncertainty of this particular detector setup was about $\pm 20\,\mu$m. The edge-to-90 %-efficiency interval with and without extrapolation smearing can only be crudely estimated to be $(37 \pm 20)\,\mu$m and $(28 \pm 20)\,\mu$m, respectively.

2013 JINST 8 P06009

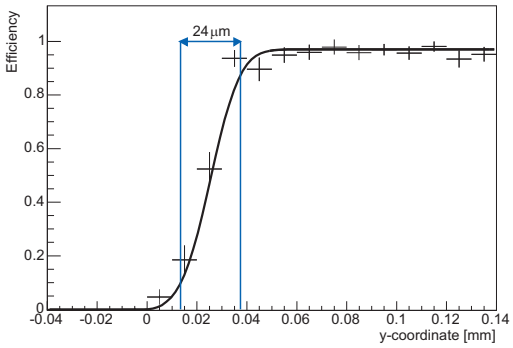

Figure 13. The reconstructed efficiency profile of the 3D active edge. The blue lines show the (10−90)% efficiency rise interval. The physical detector edge lies at $y = 0$ with a large metrology error of $\pm 20\,\mu$m.

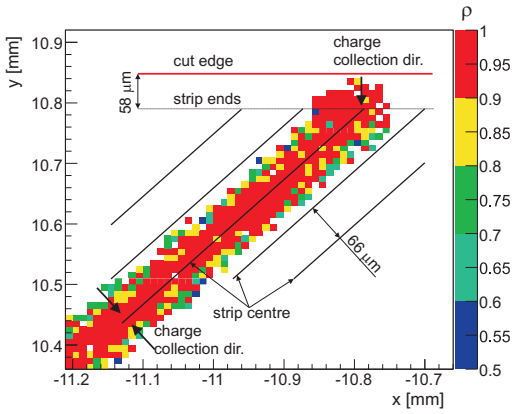

Figure 14. Charge sharing profile map of an individual strip of CTS detector 11. The colour scale quantifies the fraction ρ of the cluster charge collected by the main cluster strip (see text) as a function of the impact point. From the gradient of ρ the direction of charge collection can be deduced.

5.3 Charge sharing

Depending on the particle impact point on the detector, the charge generated may be distributed over several adjacent strips, creating multi-strip signal clusters. This charge sharing can be quantified by the fraction ρ of the cluster charge collected by the main strip, i.e. the one having the highest signal: $\rho = Q_{\text{Mainstrip}}/Q_{\text{Cluster}}$. The charge sharing profile maps in figures 14 (CTS detector) and 15 (3D-planar detector) show the mean value of ρ as a function of the impact point (x,y) given by the reference detectors. To reduce statistical fluctuations, the data of all parallel strips have been superimposed. Generally, the amount of charge sharing is low, which corresponds to ρ values close to 1.

For the CTS detector, significant charge sharing is only visible in a $\sim 10\,\mu$m-wide area located in the middle between adjacent strips. The width of the strip charge collection area is slightly enlarged due to the reference detectors' interpolation smearing of $\sim 10\,\mu$m. From the charge sharing profile the direction of charge collection can be inferred by calculating the gradient of ρ. In the regions far from the edge, the charge is collected, as expected, in directions perpendicular to the strips. However, in the edge area, the direction of strip charge collection is observed to be orthogonal to the edge, which indicates that the charge is collected from areas not geometrically covered by the strips.

2013 JINST 8 P06009

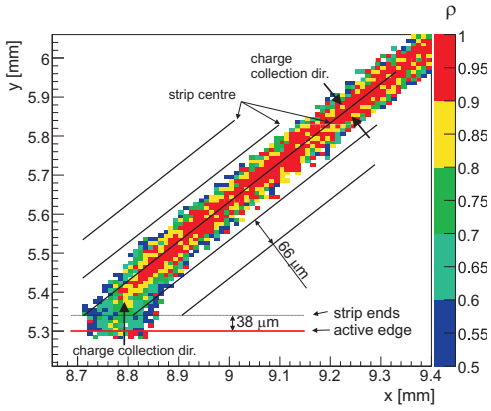

Figure 15. Charge sharing profile map of one strip of a 3D-planar detector, analogous to figure 14.

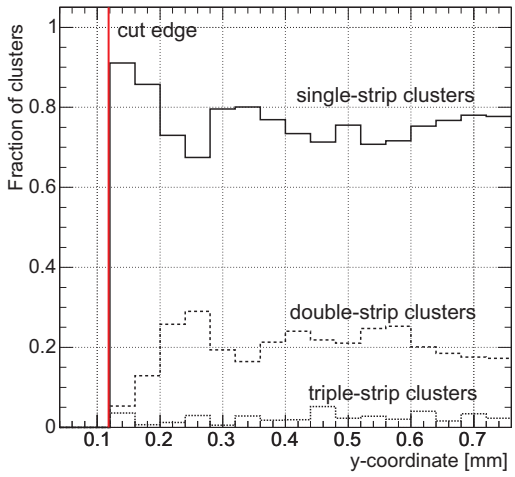

Figure 16. Cluster size in the vicinity of the CTS edge as a function of the distance y perpendicular to the edge. The solid line represents the single-strip clusters while the dashed and dotted lines show the double- and triple-strip clusters.

The 3D-planar detector exhibits two regions with increased charge sharing: (a) the narrow bands in the middle between adjacent strips, like in the CTS case; (b) the region between the active edge and the strip ends. Since the 3D implant at the cut edge is at the same potential as the back-plane electrode, the reverse bias voltage is directly applied to the 33 μm wide volume between the strips and the 5 μm thick active edge. Such a high potential difference over a small distance creates a high electric field orthogonal to the edge (and at 45° with respect to the strips — see figure 4), which is responsible for the observed charge collection direction. The long charge collection path following the curved field lines from the active edge to the strips on the detector surface enhances diffusion and thus charge sharing with neighbouring strips.

5.4 Cluster size

The hit cluster size, i.e. the number of adjacent strips with a signal above threshold, is a direct consequence of the charge sharing discussed in the previous section. Figures 16 and 17 give the

2013 JINST 8 P06009

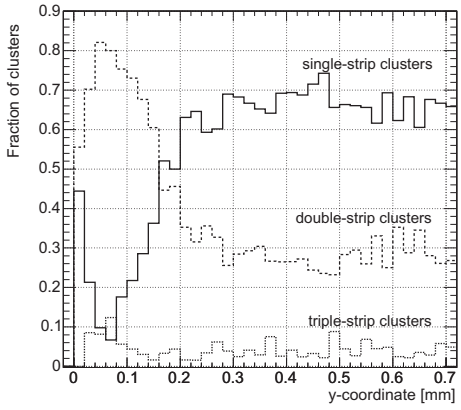

Figure 17. Cluster size in the vicinity of the 3D active edge as a function of the distance y perpendicular to the edge. The solid line represents the single-strip clusters while the dashed and dotted lines show the double- and triple-strip clusters.

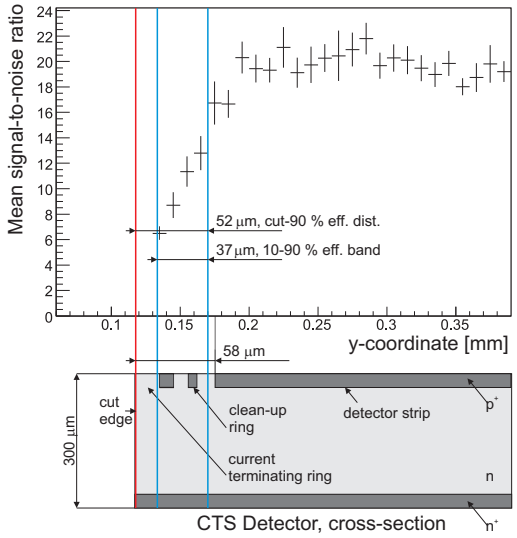

Figure 18. CTS detector 11 signal-to-noise profile near the edge (top), and the corresponding detector cross-section (bottom).

observed fractions of single-, double- and triple-strip clusters as a function of the distance from the edge for the CTS and the 3D-planar detectors, respectively.

At distances above 0.2 mm, single-strip clusters represent 70 to 80 % for CTS detectors and about 65 % for 3D-planar detectors. The slightly bigger average cluster size in the 3D-planar detector under test was caused by the lower bias leading to a longer charge collection time and more diffusion.

In the vicinity of the edge (< 0.2 mm) the ratio of single to multi-strip clusters differs substantially for the CTS and the 3D-planar detectors, which can be explained by the charge collection. The mean signal-to-noise ratio, proportional to the collected charge, is given in figures 18 and 19 in the edge area. The signal decrease in the vicinity of the cut edge is more visible for the CTS

2013 JINST 8 P06009

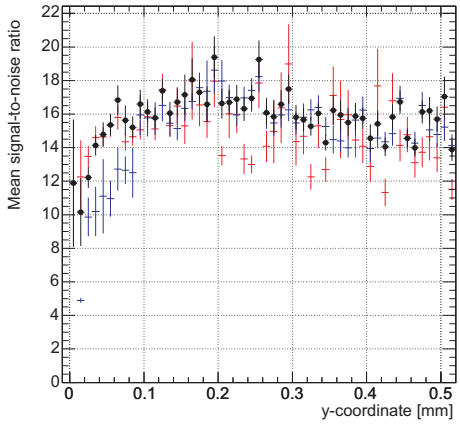

Figure 19. 3D-planar detector signal-to-noise profile near the active edge. Blue = single-strip clusters, red = double-strip clusters, black with filled circles = all clusters.

than for the 3D-planar design. In the CTS detector the bias voltage is applied by the punch-through mechanism putting the guard rings and the strips to about the same potential. Thus the charge generated in the vicinity of the cut edge is distributed between the current terminating ring, the clean-up ring and the detector strips. For impacts close to the edge, only a small portion of the charge is collected by the strips. Consequently, the mean signal-to-noise decreases from 20 in the detector bulk to only 6 at the edge. Due to this reduced cluster charge at the edge, the signals in the neighbours of the main strip tend to be below threshold. Hence single strip clusters are favoured and dominate at 90 %.

The situation is different for the 3D-planar detector (figure 19). Far from the edge, at $y > 300\,\mu$m, about 65 % of clusters consist of one strip. From $y \sim 300\,\mu$m to the strip ends at $y = 38\,\mu$m the field lines are more and more bent by the vicinity of the active edge, favouring dispersion during charge collection and hence increasing the charge sharing among adjacent strips (section 5.3). For $y < 160\,\mu$m the double-strip clusters constitute the majority (up to 80 %). In contrast to the CTS detectors, the charge generated near the end of the strips is not shared with any non-read-out ring electrodes but collected entirely by the strips, avoiding any major signal losses. For $y < 38\,\mu$m, from the strip ends to the active edge, the number of single-strip clusters increases again, although charge sharing still keeps the double-strip clusters in the majority. This trend towards single-strip clusters despite high diffusion is related to a slight reduction in collected charge, also visible in the signal-to-noise ratio, that keeps the signals of neighbour strips in a cluster below threshold. The incomplete charge collection is hypothesised to be caused by under-depletion in the low-field corner volume between the back plane and the active edge.

5.5 Impact point reconstruction performance

As discussed in section 5.3, the charge drift in the region between the strip ends and the detector edge has a component perpendicular to the edge, i.e. tilted by 45° with respect to the strips. This leads to a bias on the reconstructed impact point. In figures 20 and 21, the track residual profile is given as a function of the distance from the edge for both detector designs. The points show the mean residual values (reconstructed impact point − track intercept with the detector) while

2013 JINST 8 P06009

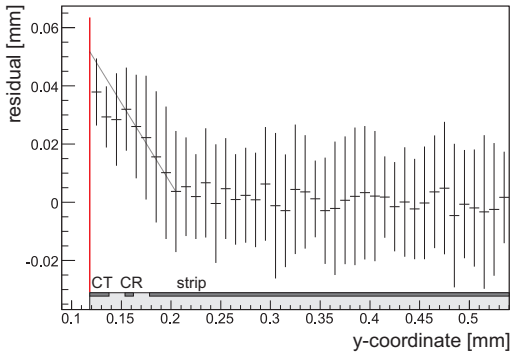

Figure 20. Mean residual values as a function of the distance from the edge of CTS detector 11. The error bars represent the resolution.

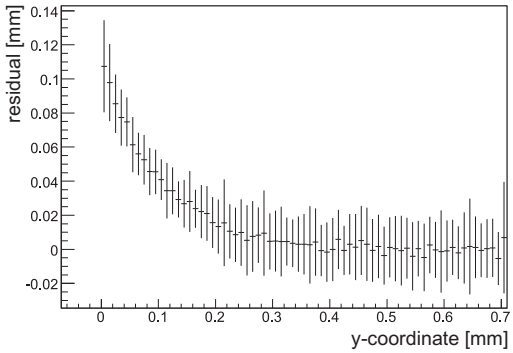

Figure 21. Mean residual values as a function of the distance from the edge of the 3D-planar detector. The error bars represent the resolution.

the bars indicate the rms of the residual distribution (about 18 μm). The shift of the reconstructed points towards the detector bulk is most pronounced for impact points between the cut edge and the area covered by strips. It could be fully corrected in software procedures based on beam tests or calibration runs.

For the CTS detectors, the bias amounts to about 40 μm at the edge, decreases approximately linearly with the distance from the edge and vanishes after about 80 μm. The observed phenomenon is in agreement with the cut-edge electric field measurements reported in [18, 19].

In the case of the 3D planar sensor (figure 21), the field towards the edge is even larger than for the CTS sensor, leading to a more pronounced shift of the coordinate towards the edge. The 3D-planar sensor shows a reconstruction offset of up to 100 μm. The effect extends to about 300 μm from the active edge.

The reconstruction resolution, represented by the error bars in figures 20 and 21, depends on the cluster size. For both detector types, the resolution far away from the sensitive edge is determined by the dominant single-strip clusters and hence amounts to about $18\,\mu\text{m} \sim 66\,\mu\text{m}/\sqrt{12}$. In the 3D-planar detectors, the strong position dependence of the cluster size leads to an improved resolution in the region between 40 and 160 μm from the edge, whereas in the CTS detectors the resolution variation is much less pronounced.

2013 JINST 8 P06009

6 Conclusions

The final size prototypes of the TOTEM CTS-planar microstrip silicon detectors (66 μm pitched and 300 μm thick) were tested in a $\sim$100 GeV muon beam, in the SPS X5 area at CERN. The test telescope was aligned with a precision of $\sim 1\,\mu$m and had an interpolation resolution of $\sim 9\,\mu$m. The insensitive area of the CTS planar silicon detectors, quantified by the distance between the detector edge and the point where 90 % of the plateau efficiency is reached, was measured to be 47 μm on average. The results of the beam tests are in good agreement with the CTS edge simulations and measurements reported in [17–19]. The measured resolution of the CTS planar devices — about 18 μm — is compatible with the expected value. The observed detection efficiency was about 95 %. The 5 % inefficiency was mainly caused by some dead and noisy strips due to bonding problems. During the edge efficiency studies, the prototype CTS detectors were biased with only 40 V, giving on average a most probable signal-to-noise value of 18. Subsequent tests of the same sensors with higher bias voltage revealed that a value of 27 is reached at 100 V. The charge collection mechanism below the CTS structure and the strips tilted by 45° result in an impact point reconstruction bias of up to 40 μm in the region adjacent to the edge. This small shift does not pose any problem for the proton track reconstruction. If needed, it could be fully corrected for.

In addition to the CTS-planar detectors, the collaboration has also studied prototype 3D-planar microstrip silicon detectors. The efficiency at the edge was observed to rise from 10 to 90 % within 7 μm. The impact point reconstruction bias at the edge was measured to reach 100 μm. In the bulk area the detectors show the expected resolution of 17 μm determined by the strip pitch. The first 3D-planar prototypes were manufactured in only 220 μm thick wafers which results in a lower signal-to-noise ratio than achievable with standard, 300 μm thick, wafers.

The tests have demonstrated that the planar detectors with two new and innovative designs of the detector edge were fully operational and reliable. In the final design, the TOTEM Roman Pots have been equipped with the CTS sensors read out via digital VFAT chips. They are successfully operating in the LHC.

References

[1] TOTEM collaboration, V. Berardi et al., *Total cross-section, elastic scattering and diffraction dissociation at the Large Hadron Collider at CERN: TOTEM Technical Design Report*, CERN-LHCC-2004-002 (2004);
TOTEM collaboration, V. Berardi et al., *Total cross-section, elastic scattering and diffraction dissociation at the Large Hadron Collider at CERN: Addendum to the TOTEM Technical Design Report*, CERN-LHCC-2004-020 (2004).

[2] TOTEM collaboration, G. Anelli et al., *The TOTEM Experiment at the CERN Large Hadron Collider*, 2008 *JINST* **3** S08007.

[3] H. Niewiadomski, *Reconstruction of Protons in the TOTEM Roman Pot Detectors at the LHC*, Ph.D. Thesis, Manchester University, Manchester U.K. (2008).

[4] TOTEM collaboration, G. Ruggiero et al., *Planar edgeless silicon detectors for the TOTEM experiment*, *IEEE Trans. Nucl. Sci.* **52** (2005) 1899 [INSPIRE].

[5] TOTEM collaboration, G. Ruggiero et al., *Final size planar edgeless silicon detectors for the TOTEM experiment*, *Nucl. Instrum. Meth.* **A 563** (2006) 41 [physics/0612105] [INSPIRE].

2013 JINST 8 P06009

[6] C. Kenney et al., *Active-edge planar radiation sensors*, *Nucl. Instrum. Meth.* **A 565** (2006) 272 [INSPIRE].

[7] S.I. Parker, C.J. Kenney and J. Segal, *3D A proposed new architecture for solid-state radiation detectors*, *Nucl. Instrum. Meth.* **A 395** (1997) 328 [INSPIRE];
C. Kenney, S. Parker, J. Segal and C. Storment, *Silicon detectors with 3D electrode arrays fabrication and initial test results*, *IEEE Trans. Nucl. Sci.* **46** (1999) 1224;
C. Kenney, S. Parker and E. Walckiers, *Results from 3-D silicon sensors with wall electrodes: near-cell-edge sensitivity measurements as a preview of active-edge sensors*, *IEEE Trans. Nucl. Sci.* **48** (2001) 2405.

[8] C. Da Via et al., *Radiation hardness properties of full-3D active edge silicon sensors*, *Nucl. Instrum. Meth.* **A 587** (2008) 243 [INSPIRE].

[9] C. Da Via et al., *3D active edge silicon sensors with different electrode configurations: Radiation hardness and noise performance*, *Nucl. Instrum. Meth.* **A 604** (2009) 505 [INSPIRE].

[10] C. Da Via et al., *3D active edge silicon detector tests with 120-GeV muons*, *IEEE Trans. Nucl. Sci.* **56** (2009) 505 [INSPIRE].

[11] TOTEM collaboration, M. Deile et al., *Tests of a Roman Pot prototype for the TOTEM experiment*, *Conf. Proc.* **C 0505161** (2005) 1701 [physics/0507080] [INSPIRE].

[12] L. Jones, *APV25-S1 User Guide Version 2.2*, September 2001.

[13] M. Raymond et al., *The APV25 0.25 µm CMOS readout chip for the CMS tracker*, *IEEE Nucl. Sci. Symp. Conf. Rec.* **2** (2000) 9/113.

[14] P. Aspell et al., *A front-end system on chip providing fast trigger information and digitized data storage for the charge sensitive readout of multi-channel silicon and gas particle detectors*, *IEEE Nucl. Sci. Symp. Conf. Rec.* **2008** (2008) 1489.

[15] C. Foudas et al., *The CMS tracker readout front end driver*, *IEEE Trans. Nucl. Sci.* **52** (2005) 2836.

[16] R. Turchetta, *Spatial resolution of silicon microstrip detectors*, *Nucl. Instrum. Meth.* **A 335** (1993) 44 [INSPIRE].

[17] E. Noschis, *Planar Edgeless Detectors for the TOTEM Experiment at the Large Hadron Collider*, Ph.D. Thesis, University of Helsinki, Helsinki Finland (2006).

[18] TOSTER Project, INTAS Collaborative Call with CERN 2005, ref. Nr 05-103-7533.

[19] E. Verbitskaya et al., *Advanced Model of Silicon Edgeless Detector Operation*, *IEEE Nucl. Sci. Symp. Conf.* **2008** (2008) 2711.

2013 JINST 8 P06009